Monthly Notices
of the
ROYAL ASTRONOMICAL SOCIETY

MNRAS **494,** 396–410 (2020)
Advance Access publication 2020 March 30

doi:10.1093/mnras/staa703

Asymmetric spatial distribution of subsolar metallicity stars in the Milky Way nuclear star cluster

A. Feldmeier-Krause [1]★ W. Kerzendorf [2,3] T. Do,[4] F. Nogueras-Lara [5] N. Neumayer,[5] C. J. Walcher,[6] A. Seth,[7] R. Schödel,[8] P. T. de Zeeuw,[9,10] M. Hilker,[11] N. Lützgendorf,[12] H. Kuntschner[11] and M. Kissler-Patig[13]

[1]*The University of Chicago, The Department of Astronomy and Astrophysics, 5640 S. Ellis Ave, Chicago, IL 60637, USA*
[2]*Department of Physics and Astronomy, Michigan State University, East Lansing, MI 48824, USA*
[3]*Department of Computational Mathematics, Science, and Engineering, Michigan State University, East Lansing, MI 48824, USA*
[4]*UCLA Galactic Center Group, Physics and Astronomy Department, UCLA, Los Angeles, CA 90095, USA*
[5]*Max Planck Institute for Astronomy, Königstuhl 17, D-69117 Heidelberg, Germany*
[6]*Leibniz-Institut für Astrophysik Potsdam (AIP), An der Sternwarte 16, D-14482 Potsdam, Germany*
[7]*Department of Physics and Astronomy, University of Utah, Salt Lake City, UT 84112, USA*
[8]*Instituto de Astrofísica de Andalucía (CSIC), Glorieta de la Astronomía s/n, E-18008 Granada, Spain*
[9]*Sterrewacht Leiden, Leiden University, Postbus 9513, NL-2300 RA Leiden, The Netherlands*
[10]*Max-Planck-Institut für Extraterrestrische Physik, D-85748, Garching, Germany*
[11]*European Southern Observatory (ESO), Karl-Schwarzschild-Straße 2, D-85748 Garching, Germany*
[12]*European Space Agency, c/o STScI, 3700 San Martin Drive, 21218 Baltimore, MD, USA*
[13]*European Space Agency – European Space Astronomy Centre, Camino Bajo del Castillo s/n, E-28692 Villanueva de la Ca nada, Madrid, Spain*

Accepted 2020 March 5. Received 2020 March 5; in original form 2019 September 18

ABSTRACT

We present stellar metallicity measurements of more than 600 late-type stars in the central 10 pc of the Galactic Centre. Together with our previously published KMOS data, this data set allows us to investigate, for the first time, spatial variations of the nuclear star cluster's metallicity distribution. Using the integral-field spectrograph KMOS (VLT), we observed almost half of the area enclosed by the nuclear star cluster's effective radius. We extract spectra at medium spectral resolution and apply full spectral fitting utilizing the PHOENIX library of synthetic stellar spectra. The stellar metallicities range from [M/H] $= -1.25$ dex to [M/H] $> +0.3$ dex, with most of the stars having supersolar metallicity. We are able to measure an anisotropy of the stellar metallicity distribution. In the Galactic north, the portion of subsolar metallicity stars with [M/H] < 0.0 dex is more than twice as high as in the Galactic south. One possible explanation for different fractions of subsolar metallicity stars in different parts of the cluster is a recent merger event. We propose to test this hypothesis with high-resolution spectroscopy and by combining the metallicity information with kinematic data.

Key words: Stars: late-type – Galaxy: centre – infrared: stars.

1 INTRODUCTION

The Milky Way nuclear star cluster consists of tens of millions of stars, densely packed in a small region at the centre of our Galaxy. The cluster extends over $r_e = 4$–5 pc (Schödel et al. 2014a; Fritz et al. 2016), with a mass of about 2×10^7 $M_\odot$ (Schödel et al. 2014a; Feldmeier-Krause et al. 2017b). The stars in the nuclear star cluster belong to several stellar populations, they cover ages of few Myr to several Gyr, with most of the stars being more than 5 Gyr old (Blum et al. 2003; Pfuhl et al. 2011), and metallicities from subsolar to supersolar. Unlike the stellar age, metallicities can be measured directly from individual stellar spectra. This makes metallicities a useful tool to separate different stellar populations and understand the formation history of the nuclear star cluster.

The first metallicity measurements of cool stars in the nuclear star cluster consisted of small samples. Due to the high extinction, traditional methods for determining metallicities with optical spectroscopy cannot be applied in the Galactic Centre, and for this reason, metallicity measurements are based on *K*-band or *H*-band spectroscopy. Carr, Sellgren & Balachandran (2000), Ramírez et al. (2000), and Davies et al. (2009) analysed high-resolution spectra and obtained solar to slightly supersolar iron-based [Fe/H] for less than 10 stars, most of them red supergiants. Cunha et al. (2007)

★ E-mail: afeldmei@uchicago.edu

studied 10 supergiants in the central 30 pc and found a narrow, slightly supersolar metallicity distribution with enhanced [α/Fe] ($\sim$0.2–0.3 dex). Supergiant stars are relatively young, $\lesssim$1 Gyr, and rare. Red giant stars are better suited to study the metallicity distribution of stars in the nuclear star cluster, as red giants are older, abundant, and bright enough for spectroscopic observations.

In the past years, several studies measured metallicities of red giant stars in the nuclear star cluster. Do et al. (2015) analysed spectra of 83 red giant stars with medium spectral resolution ($R \sim 5400$) and measured the overall metallicity [M/H]. They found a broad metallicity distribution, ranging from subsolar ([M/H] < -1 dex) to metal-rich stars ([M/H] $> +0.5$ dex). The majority of the stars has supersolar metallicity ([M/H] > 0 dex). This finding was confirmed by Feldmeier-Krause et al. (2017a) on a larger sample of 700 stars and similar methods ($R \sim 4\,000$). Rich et al. (2017) studied a sample of 17 stars but higher spectral resolution ($R \sim 24\,000$). They measured the iron-based metallicity [Fe/H] and obtained not only a median value of -0.16 dex but also a large spread from subsolar to supersolar metallicities. These studies confirm the complex star formation history of the nuclear star cluster.

In order to fully understand the formation and history of the nuclear star cluster, it is important to understand the metallicity distribution of the stars in the cluster and if there are any spatial variations. We extended our previous work presented in Feldmeier-Krause et al. (2017a), where we measured the metallicity distribution of the central 4 pc^2 (radial range: 0.1–1.4 pc) of the nuclear star cluster, by additional data. Both data sets were observed and analysed with an identical observational setup. The new data set presented here covers an area that is larger by a factor of 5.6 at a radial range of 0.4–4.9 pc from the centre. The combined data set covers 26.7 pc^2, which is about half of the area enclosed by the effective radius (assuming 4.2 pc, Schödel et al. 2014a). The data extend approximately along the Galactic plane, reaching to the effective radius r_e in the north-west and south-east. Our data set allows us to study, for the first time, spatial variations of the metallicity distribution within the Milky Way nuclear star cluster.

This paper is organized as follows: We present our data set in Section 2 and describe our spectral analysis in Section 3. In Section 4, we present our results of the metallicity distribution and discuss them in Section 5. Our conclusions follow in Section 6.

2 DATA SET

2.1 Observations

Our spectroscopic observations were performed with KMOS (Sharples et al. 2013) on VLT-UT1 (Antu) in 2014, in the nights of April 10, 12, and 24, May 11 and 31, and June 6 in service mode. KMOS is a multiobject spectrograph with 24 integral field units (IFUs), which can be arranged in a close configuration. With 16 dithers in this close configuration, it is possible to observe a mosaic covering 64.9 arcsec $\times$ 43.3 arcsec. We observed six mosaic fields of the Milky Way nuclear star cluster, within its half-light radius ($r_e = 110$ arcsec $= 4.2$ pc, Schödel et al. 2014a). We chose the location of the fields such that we extended Field 0 (Feldmeier-Krause et al. 2017a) to obtain approximately symmetric coverage toward Galactic east and west, while avoiding the region of higher extinction in the Galactic south-west. The region covered by our data is shown in Fig. 1.

Depending on the distance from the centre of the cluster, we chose exposure times of 155 s or 190 s. The exposure time is shorter closer to the centre to prevent persistence and saturation. Each field was observed twice; this means that we have in total 12 mosaics. In some of the nights, different IFUs had technical problems and were not used, causing several of the mosaics to have holes. For that reason, we observed the two mosaics of the same field with different rotator angles, 120° and $-60°$ (except for Field 2, for which both mosaics have the same rotator angle). Rotating the mosaics by 180° makes sure that inactive IFUs fall on different regions of the sky, and we have at least one exposure of each region. We extracted and analysed spectra from each exposure separately. If we had more than one exposures of a star, we took the mean of the stellar parameter measurements.

We observed in the near-infrared K band ($\sim$19 340–24 600 Å), where the spectral resolution is about 4000. The spatial sampling is 0.2 arcsec pixel^{-1} $\times$ 0.2 arcsec pixel^{-1}, the sampling along the dispersion axis is $\sim$2.8 Å; pixel^{-1}. We made offsets to a dark cloud (G359.94+0.17, $\alpha \approx 266°.2$, $\delta \approx -28°.9$; Dutra & Bica 2001) for sky observations, with the same exposure time as on source. For telluric corrections, we observed B-type dwarf stars. We summarize our observations in Table 1. We additionally list Field 0, which was observed in 2013 September. The observations and results of this field were already presented in Feldmeier-Krause et al. (2015) and Feldmeier-Krause et al. (2017a). This field covers the very centre of the Milky Way nuclear star cluster, and we used it for comparison.

2.2 Data reduction

Our data reduction procedure is similar to the reduction of the central field, described in Feldmeier-Krause et al. (2015). We used the KMOS pipeline (Davies et al. 2013) provided by ESO with EsoRex (ESO Recipe Execution Tool). The reduction steps include dark subtraction, flat-fielding, wavelength calibration, illumination correction using the flat-field exposures, and telluric correction with a standard star. Before telluric correction, we removed the intrinsic stellar absorption lines and the blackbody spectrum from the standard star spectrum with our own IDL routine. After these reduction steps, the object and sky exposures were reconstructed to data cubes. We combined the two sky frame exposures of each observing block to a master sky frame and subtracted the sky by scaling it to the object cubes, as described by Davies (2007). Cosmic rays were removed with an IDL program for data cubes (Davies et al. 2013) based on the program L.A.COSMIC (van Dokkum 2001).

We have complimentary photometric catalogues in J, H, and K_S bands in the field and extinction maps provided by Nogueras-Lara et al. (2018) and Nogueras-Lara et al. (2019a). The imaging observations were done with HAWK-I in speckle holography mode, which ensures a high spatial resolution and completeness. For 18 bright stars with no HAWK-I photometry due to saturation, we used SIRIUS K_S-band photometry (Nishiyama et al. 2006). The star catalogue is used to extract stellar spectra. For the central field (see Feldmeier-Krause et al. 2015, 2017a), we used the program PAMPELMUSE (Kamann, Wisotzki & Roth 2013); however, for the observations analysed in this paper, this was not feasible. PAMPELMUSE performs point spread function (PSF) fitting and light deconvolution in crowded fields. It requires exposures of several stars to fit the PSF. Due to the lower stellar density compared to the central field, there were not enough stars in a single exposure for a PSF fit. We could not combine several subsequently taken exposures, as observing conditions varied too much. Instead of using PAMPELMUSE, we only extracted stars that are isolated from nearby stars to avoid blending of extracted spectra. We used a k-d-tree algorithm to identify stars in the photometric catalogue with no

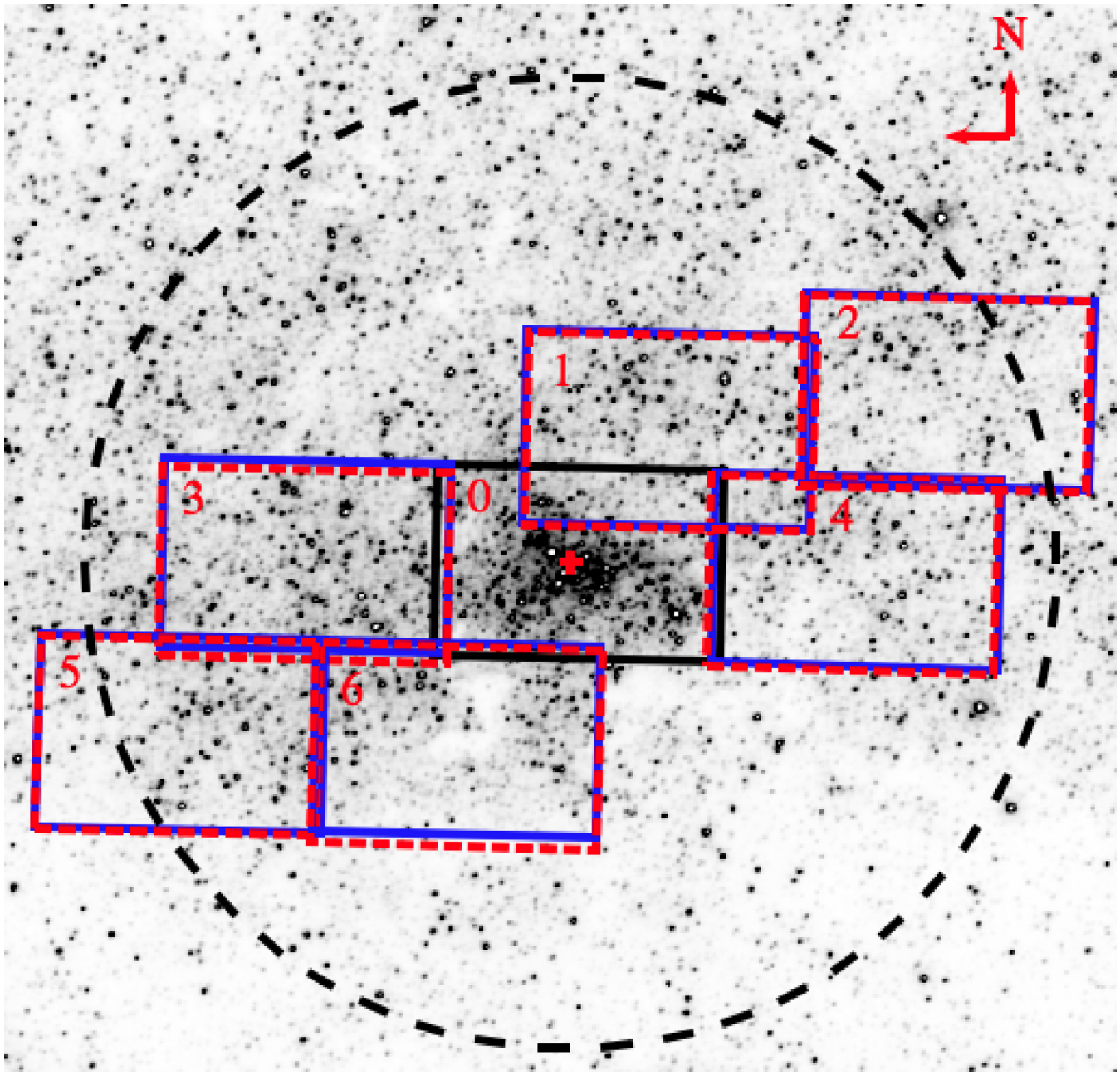

Figure 1. The region covered by our KMOS observations. We observed six fields (labelled from 1 to 6) out to the effective radius $r_e = 110$ arcsec $= 4.2$ pc, which is denoted by the black dashed circle. The central Field 0 was presented in Feldmeier-Krause et al. (2015) and Feldmeier-Krause et al. (2017a). The red cross denotes the position of the supermassive black hole. The underlying image is from the VISTA Variables in the Via Lactea Survey (Saito et al. 2012) in K_S band, Galactic north is up, and Galactic east is to the left. The blue and red dashed boxes indicate the repeated observations per mosaic field.

neighbour within six KMOS pixels (i.e. 1.″2), unless the neighbour stars are fainter by at least 3 mag in the K_S band. We extracted spectra of such stars within a circular aperture with a 3 pixel (0.6 arcsec) radius by simply adding the flux within the aperture. We also subtracted the background flux determined from a 2 pixel (0.4 arcsec) wide annulus at a radius of >4 pixel (0.8 arcsec). For a fair comparison, we used this method to re-extract spectra in the central field and re-analyse the spectra. We found consistent results with Feldmeier-Krause et al. (2017a). Depending on the stellar density of the field and the number of active IFUs at the time of the observations, we extracted about 190–320 spectra per individual mosaic. We note that these numbers include foreground stars, multiple exposures of the same star, and low signal-to-noise spectra. We corrected the velocity scale of the spectra to the local standard of rest.

As noted by Gazak et al. (2015), the spectral resolution of the 24 KMOS IFUs varies spatially, both for different IFUs and for individual IFUs, with a mean value of $R = \lambda/\Delta\lambda = 4\,200$. Within one IFU, the spectral resolution R can have a standard deviation of up to 150, and over all IFUs, the standard deviation is about 300. We measured the line-spread function on the reconstructed sky data cubes, as described in Feldmeier-Krause et al. (2017a). We fitted

Table 1. Summary of KMOS observations.

Field	Mosaic	Night	Exposure time (s)	Seeing (arcsec)	Rotator angle (deg)	Inactive IFU	RA (deg)	Dec (deg)
1	1	10. April 2014	155	0.6–0.9	−60	–	266.405	−29.009
	2	10. April 2014	155	0.6–0.9	120	–	266.405	−29.009
2	1	11. May 2014	190	0.9–1.2	120	4	266.392	−29.022
	2	11. May 2014	190	0.9–2.5	120	4	266.392	−29.022
3	1	31. May 2014	155	0.7–1.5	−60	4, 11	266.427	−28.993
	2	6. June 2014	155	0.6–0.8	120	4, 11,15	266.427	−28.993
4	1	6. June 2014	155	0.7–1.1	−60	4, 11,15	266.407	−29.023
	2	6. June 2014	155	0.9–1.3	120	4, 11,15	266.407	−29.023
5	1	12. April 2014	190	0.9–1.2	−60	–	266.442	−28.992
	2	24. April 2014	190	0.9–1.4	120	–	266.442	−28.992
6	1	12. April 2014	155	1.1–1.8	−60	–	266.432	−29.008
	2	12. April 2014	155	1.0–1.6	120	–	266.432	−29.008
0	1	23. Sept. 2013	100	0.7–0.9	120	13	266.417	−29.007
	2	23. Sept. 2013	100	1.0–1.4	120	13	266.417	−29.007

Gaussian functions to several sky lines in the wavelength region $\lambda = 21\,900$–$22\,400$ Å and created spatially resolved resolution maps for the 24 IFUs. These will be used for the full spectral fitting performed in Section 3.2.

3 ANALYSIS

In this section, we describe the different analysis steps to measure stellar parameters. We derived radial velocities using a large spectral range before we measured spectral indices. Then, we applied full spectral fitting to derive the stellar parameters metallicity [M/H], effective temperature $T_{\rm eff}$, and surface gravity $\log(g)$.

3.1 Measuring kinematics and spectral indices

We fitted the stellar spectra in the wavelength region of 20 880–23 650 Å; with the IDL program PPXF (Cappellari & Emsellem 2004) to measure the stellar radial velocity. We used the high-resolution spectra of late-type stars by Wallace & Hinkle (1996) as templates and convolved them to the mean spectral resolution of the KMOS spectra. The stellar spectra contain several gas emission lines, which originate from the interstellar gas inside the Milky Way nuclear star cluster: In the central 2 pc of the Milky Way nuclear star cluster, there is the so-called 'minispiral' or Sgr A West (see e.g. Paumard, Maillard & Morris 2004; Kunneriath et al. 2012). It is visible in the Br γ (21 661 Å) and He I (20 587 Å) transitions in emission (see figs. 7 and 8 in Feldmeier-Krause et al. 2015). Further out, in the central 6 pc of the Milky Way, there is a clumpy circumnuclear ring (see e.g. Requena-Torres et al. 2012; Feldmeier et al. 2014), which emits at several H_2 transitions, e.g. 21 218 Å, 22 235 Å, and 22 477 Å. We masked the wavelength regions of emission lines and several sky emission lines in the PPXF fit. As result, we obtained the radial velocity of the star and additionally the velocity dispersion. The velocity dispersion has no physical meaning. As we fit single stars, it is usually low. However, it can reach high values, which indicates a bad fit of a low signal-to-noise spectrum. We measured the uncertainties by running Monte Carlo simulations and adding noise to the spectra. The radial velocity was later used as prior information for the full spectral fitting.

The strength of different absorption lines can be used to estimate effective temperatures and thus differentiate cool late-type stars from hot early-type stars. Further, it is possible to differentiate red supergiant from red giant stars. We measured spectral indices to constrain the possible ranges of effective temperature and surface gravity. We measured the equivalent width of the first CO band head (∼22 935 Å) and the Na I doublet (22 062 Å and 22 090 Å), with the index definitions of Frogel et al. (2001), after correcting the spectra to the rest frame.

3.2 Full spectral fitting

In order to constrain the stellar parameters, we fitted the stellar spectra of our KMOS data set. We used the STARKIT code developed by Kerzendorf & Do (2015). This code was also used by Do et al. (2015) and Feldmeier-Krause et al. (2017a). STARKIT applies Bayesian sampling (Feroz, Hobson & Bridges 2009; Buchner et al. 2014). The code uses a grid of synthetic spectra and interpolates them to find the best-fitting stellar parameter to a stellar spectrum.

As in Feldmeier-Krause et al. (2017a), we used the PHOENIX spectral library (Husser et al. 2013) of synthetic spectra. The synthetic spectra are in a grid with $T_{\rm eff} = (2\,300$ K; 12 000 K), and a step size of $\Delta T_{\rm eff} = 100$ K, [M/H] = [−1.5 dex, +1.0 dex], Δ [M/H] = 0.5 dex, $\log(g) = [0.0$ dex, 6.0 dex], and $\Delta\log(g) = 0.5$ dex. [M/H] denotes the overall metallicity of all elements, not the Fe-based metallicity. The model spectra have [α/Fe] = 0 but [α/H] = [M/H]. We were not able to measure [α/Fe] as additional fitting parameter. Our tests resulted in subsolar to solar [α/Fe] also for stars with subsolar [M/H]. We do not consider these results reliable and believe that our spectral resolution is too low. Most absorption lines are blends of several elements, which makes it hard to constrain single element abundances. Therefore, we decided to fit only [M/H], $T_{\rm eff}$, and $\log(g)$, and assume [α/Fe] = 0. The effect of non-zero [α/Fe] on our measurements is included in our systematic uncertainties.

The model spectra were convolved to the respective spectral resolution of each KMOS spectrum, as determined by the sky lines on the location on the respective IFU (see Section 2.2). We fitted the effective temperature $T_{\rm eff}$, metallicity [M/H], surface gravity $\log(g)$, and radial velocity v_z. The fits were done in the wavelength region $\lambda = 20\,900$–$22\,900$ Å;. Some stellar spectra also have gas emission lines at Br γ (21 661 Å) and H_2 transitions at 21 218 Å and 22 235 Å. We excluded the region around the emission lines from the fit if the emission line region had a significantly higher standard deviation than the rest of the spectrum. Further,

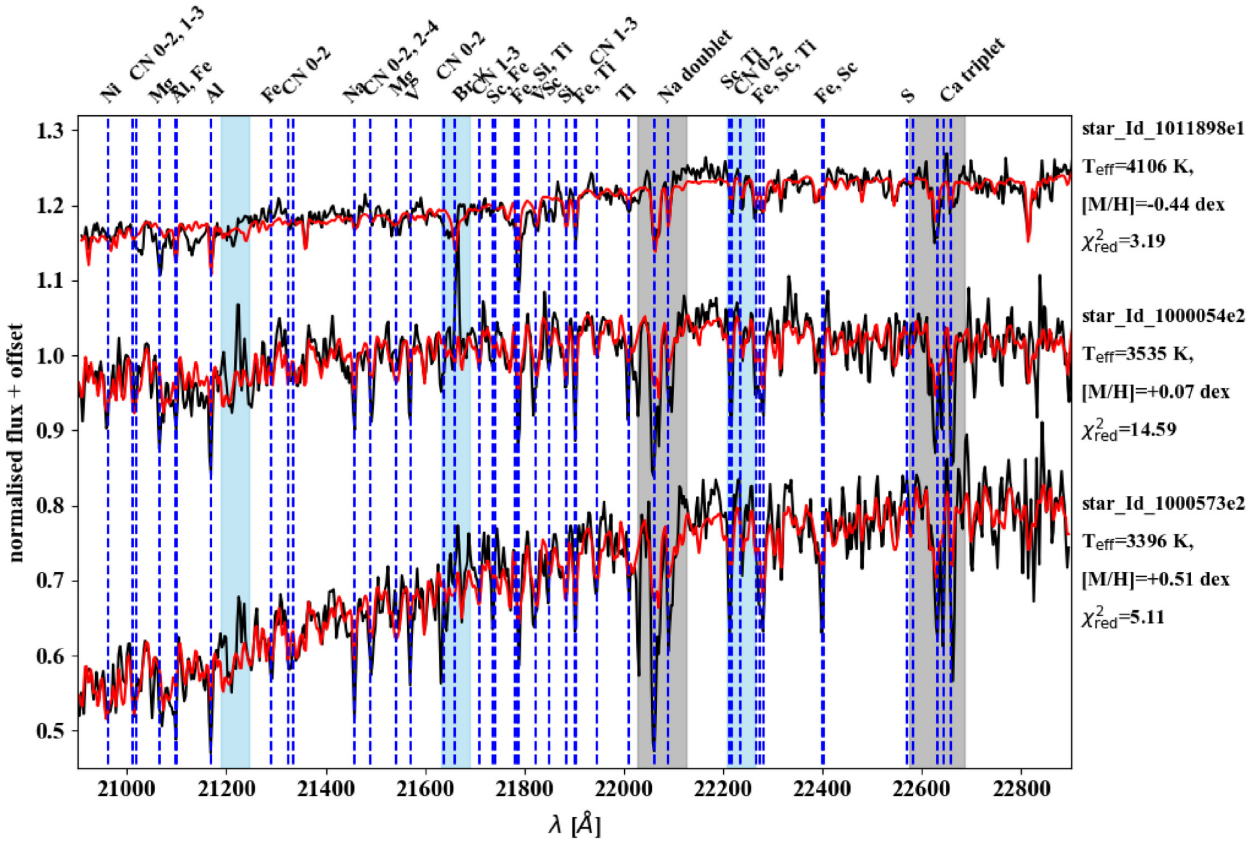

Figure 2. Spectra (black) and best-fitting model (red) of three different stars with metallicities [M/H] = −0.44, +0.07, and +0.51 dex. Blue dashed lines denote known spectral lines, labelled on top of the plot. Grey shaded areas were excluded from the fit; the light blue shaded areas were excluded for spectra with strong contamination of the Brackett-γ or H_2 gas emission lines.

we excluded the regions of the spectrum where the Na and Ca lines are [$\lambda = (22\,027$ Å, $22\,125$ Å) and $\lambda = (22\,575$ Å, $22\,685$ Å)], as Galactic Centre stars have stronger Na and Ca lines compared to normal disc stars (Blum, Sellgren & Depoy 1996; Feldmeier-Krause et al. 2017a), which biases the fit to unrealistic high metallicities. We show three spectra and their best-fitting models as examples in Fig. 2. The spectral continuum shape is influenced by extinction, which can bias the fit of the stellar parameters. For that reason, the continuum was modelled with a fifth-degree polynomial function.

We used the radial velocity measured with PPXF as prior information, with a Gaussian prior. The PPXF radial velocity was set as mean of the Gaussian and the radial velocity uncertainty as the width of the Gaussian. The magnitude of a star contains information about its luminosity class and thus constrains the possible range of the surface gravity. We corrected the magnitudes for extinction using the extinction map of Nogueras-Lara et al. (2018, fig. 30). We used the extinction corrected $K_{S,0}$-band magnitude to set constraints on the surface gravity, as done by Do et al. (2015) and Feldmeier-Krause et al. (2017a). Since brighter stars have a lower surface gravity, we set the uniform priors for stars with $K_{S,0} < 12$ mag to 0.0 dex $< \log(g) <$ 4.0 dex and for stars with $K_{S,0} \geq 12$ mag to 2.0 dex $< \log(g) <$ 4.5 dex. A further constraint comes from the equivalent width of the CO absorption line. Stars with $EW_{CO} > 25$ Å are potentially supergiants. We set the prior uniform to 0.0 dex $< \log(g) <$ 2.0 dex for stars with $EW_{CO} > 25$ Å and $K_S \leq 10$ mag and to 0.0 dex $< \log(g) <$ 4.0 dex for stars with $EW_{CO} > 25$ Å and $K_S > 10$ mag.

The effective temperature and metallicity priors were set uniform in the ranges (2300 K, 12 000 K) and (−1.5 dex, +1.0 dex), respectively. We also tested a Gaussian prior for T_{eff} on a subset of stars by using T_{eff} determined from the empirical $EW_{CO} - T_{eff}$ calibration derived in Feldmeier-Krause et al. (2017a). This increased the fitting results of T_{eff} by a median value of 33 K, whereas the median changes of the other measurements, $\log(g)$, [M/H], and v_z, were close to zero. For easier comparison with the results of Feldmeier-Krause et al. (2017a), where a uniform prior for T_{eff} was used, we decided to use the uniform prior in this study as well. But this test shows that the metallicity results are robust under moderate T_{eff} variations.

3.3 Data selection

To measure the stellar parameters, we require high signal to noise. We excluded stars with low signal-to-residual-noise (< 20) spectra, or large fitting uncertainties ($\sigma_{T_{eff}} > 250$ K, $\sigma_{[M/H]} > 0.25$ dex, $\sigma_{\log(g)} > 1$ dex, $\sigma_{v_z} > 10$ km s^{-1}). We combined the fit results obtained from individual spectra of the same star to a mean stellar parameter measurement. We have 704 stars with at least one good stellar parameter fit from 1136 analysed spectra.

However, this set includes also foreground stars. We used the photometry to determine which stars are members of the Milky Way nuclear star cluster. In particular, the extinction-corrected $(H - K_S)_0$ colour allows to identify foreground stars. The intrinsic $H - K_S$ colour of late-type stars in the nuclear star cluster is in the rather narrow range of about −0.13 mag to +0.38 mag (Do et al. 2013;

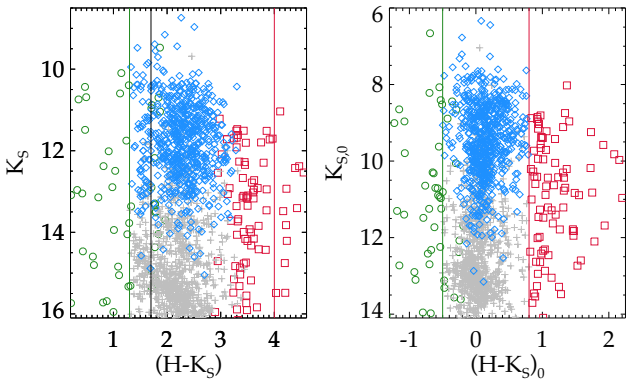

Figure 3. Colour magnitude diagrams of stars within the KMOS Fields 1–6 with extracted spectra and H and K_S photometry before (left) and after (right) extinction correction. Our sample of member stars is shown as blue diamond symbols. We classify stars with observed colours $H - K_S < 1.3$ mag or extinction-corrected colours $(H - K_S)_0 < -0.5$ mag as foreground stars (green circles) and stars with $H - K_S > 4.0$ mag or $(H - K_S)_0 > 0.8$ mag as background stars (red squares). Grey plus signs denote stars that were excluded due to our quality cuts on signal-to-noise and statistical uncertainties and red and green vertical lines show our colour cuts for member stars. We applied a different extinction map on stars left of the black vertical line at 1.3 mag $< (H - K_S) < 1.7$ mag (see text for details).

Schödel et al. 2014b). This holds for stars in our magnitude range, for metallicities from −1.0 to 0.6 dex, and for ages from 6.5 to at least 10 Gyr (Bressan et al. 2012; Chen et al. 2014; Tang et al. 2014; Rosenfield et al. 2016). If a star has a significantly bluer extinction-corrected colour $(H - K_S)_0$, it is an overcorrected foreground star. We consider stars with extinction-corrected $(H - K_S)_0 < -0.5$ mag as foreground stars. To correct for extinction, we used the extinction maps of Nogueras-Lara et al. (2018), in particular, we corrected stars with observed $H - K_S < 1.7$ mag with the extinction map derived from stars with 1.4 mag $< H - K_S < 1.7$ mag, and stars with observed $H - K_S > 1.7$ mag with the extinction map derived from stars with 1.7 mag $< H - K_S < 3.0$ mag, as shown by Nogueras-Lara et al. (2018). In addition, we consider stars with uncorrected $H - K_S < 1.3$ mag as foreground stars, following Nogueras-Lara et al. (2019b). On the other hand, stars with a redder colour are probably subject to a higher extinction and are thus potential background stars. We classify a star as potential background star if its extinction-corrected colour $(H - K_S)_0 > 0.8$ mag. We show a colour magnitude diagram of our data set in Fig. 3.

For 31 stars, we have only one band, H or K_S, or they lie in a region of the extinction map where extinction is underestimated ($b < -0.06$ deg, Nogueras-Lara et al. 2018). Hence, we cannot classify them as member stars using photometry. However, foreground stars have a steeply decreasing continuum in the K-band spectrum, whereas member stars have a rather straight or even increasing continuum slope. Thus, we can infer the member status of a given star from the spectrum. We measured the continuum slope with an outlier-resistant two-variable linear regression fit in the wavelength region ∼19 600–22 000 Å. Then, we applied machine-learning algorithms to the data set. The training set consists of about 800 stars with known membership status from using the photometry and extinction map. We included central stars (Field 0) to the training set. We used the R ENTROPY package to select useful machine-learning variables. The by far most important variable is the spectral continuum slope; however, also the y-intercept, the Na and CO equivalent widths, and RA and Dec have a small effect on the machine-learning result. This can be expected, as these properties are different for Galactic Centre stars than for foreground stars. In particular, Galactic Centre stars have rather high EW_{Na} (Blum et al. 1996; Feldmeier-Krause et al. 2017a) compared to normal disc stars. At the Galactocentric distance of 8 kpc, the member stars of our sample are M giant or supergiant stars rather than main sequence stars. This means that EW_{CO} is larger in member stars than foreground stars, which can be earlier giant stars or main sequence stars. The position of the stars on the sky has a small effect on the outcome of the machine learning and the radial velocity has the highest entropy of all considered parameters (larger by a factor of 4). This means that the radial velocity cannot differentiate foreground stars from member stars and we do not use it as variable.

We used 10-fold cross-validation and average the results to determine the classifier. We tested various classification methods with the R package and found that fitting Multinomial Log-linear Models via neural networks (function MULTINOM in package NNET) has the smallest misclassification error, 6.4 per cent. Our focus is a small false-positive rate (FPR), which denotes the ratio of foreground stars that are misclassified as member stars divided by the total number of foreground stars, rather than the false-negative rate (FNR), which is the ratio of member stars that are misclassified as foreground stars divided by the total number of member stars, because we rather discard a member star than including a foreground star in our sample. The MULTINOM classifier has FPR = 17.6 per cent and FNR = 6.2 per cent. We apply the MULTINOM classifier on the 31 stars for which we cannot determine the membership status from the photometry. We add the 29 stars that are classified as member stars to the data set. With our FPR of 17.6 per cent, it is unlikely that all the stars classified as member stars are misclassified foreground stars. We expect at most five misclassified foreground stars among the 29 stars classified as member stars. These stars are exclusively located in the region $b < -0.06$ deg, where we have no coverage from the extinction map.

There may still be contamination by stars of other Galactic components, such as the bar or halo interlopers, that are close to the nuclear star cluster and have a similar colour. We estimate the remaining contamination rate with the Besançon Galaxy Model[1] (BGM, Czekaj et al. 2014), assuming a diffuse extinction of 3.5 mag kpc^{-1}, in an area of 1 deg^2 around the nuclear star cluster. We consider the magnitude range of 9.48 mag < K < 13.19 mag, which covers the observed K-band magnitudes of stars considered in Section 4.2 and Fig. 6. With these parameters, the BGM contains only one star at a distance of 83 pc from Sgr A∗, 40 pc behind it along the line of sight, which belongs to the young thick disc. All other 469 stars of the BGM are >638 pc distant from Sgr A∗ along the line of sight. For this reason, these stars have a different colour and can be identified as foreground stars. Considering our field of view of 4.9 arcmin^2, the model predicts only 0.00136 stars that may be misidentified as member stars of the nuclear star cluster. The BGM therefore suggests that the remaining foreground star contamination in our data set is negligible.

3.4 Uncertainties

The full-spectral fitting gives statistical uncertainties σ_{fit} for the stellar parameters. However, these can be lower than the standard deviation σ_{sd} from fitting several spectra of the same star. If this

[1] https://model.obs-besancon.fr/modele_home.php

was the case, we used the standard deviation $\sigma_{\rm sd}$ of the ∼360 stars with several exposures rather than the formal fitting uncertainties $\sigma_{\rm fit}$. For the remaining ∼350 stars with only one exposure, we used the median of $\sigma_{\rm sd}$ as statistical uncertainty, if it was larger than the formal fitting uncertainty $\sigma_{\rm fit}$.

In addition, we considered systematic uncertainties. Feldmeier-Krause et al. (2017a) fitted spectra from different stellar libraries with reference stellar parameters using STARKIT. They found that the STARKIT results differ by $\langle \Delta T_{\rm eff} \rangle = -58$ K, $\langle \Delta$ [M/H]$\rangle = -0.1$ dex, and $\langle \Delta \log(g) \rangle = 0.2$ dex from the reference stellar parameters, with standard deviations $\sigma_{\Delta T_{\rm eff}} = 205$ K, $\sigma_{\Delta[{\rm M/H}]} = 0.24$ dex, and $\sigma_{\Delta \log(g)} = 1.0$ dex. The offsets and scatter are partially caused by systematics in the model spectra, by the different alpha abundances of the library stars, and by the different methods and assumptions that were made to derive the reference stellar parameters. Nevertheless, we use the standard deviations as systematic uncertainties and added them in quadrature to the statistical uncertainties. We note that the systematic uncertainties were derived by fitting stars with [M/H] < 0.3 dex. The uncertainties for the stars with higher metallicities may be underestimated. The mean total uncertainties are $\sigma_{T_{\rm eff}} = 212$ K, $\sigma_{[{\rm M/H}]} = 0.26$ dex, and $\sigma_{\log(g)} = 1.0$ dex.

As additional test of systematic uncertainties, we fitted six red giant star spectra of NGC 6388 observed with SINFONI (Lanzoni et al. 2013) at a similar spectral resolution as our data. We obtained $\langle$[M/H]$\rangle = -0.54$ dex, which is in agreement with other measurements, and the value listed in the Galactic Globular cluster catalogue by Harris (1996) and Harris (2010) of [Fe/H] = −0.55 dex. The six metallicity measurements have a standard deviation $\sigma_{[{\rm M/H}]} = 0.15$ dex. This value means that, for a monometallic stellar population, our method will have a dispersion of ∼0.15 dex, which is less than our systematic uncertainty.

Rich et al. (2017) observed 17 M giants at high spectral resolution in the Galactic Centre. We matched our data set to theirs and found three stars, which are probably the same: Their GC13282, GC11025, and GC16887 correspond to our stars Id134, Id1011914, and Id3021083. The samples have only small differences of the observed velocities (2–8.9 km s^{-1}), $K_{\rm S}$ (0.06–0.29 mag), and the coordinates (0.27–0.78 arcsec). Our results for $T_{\rm eff}$ and log (g) agree well within the uncertainties, though our results for log (g) are lower in all three cases. The metallicity is harder to compare, as we measured the total metallicity [M/H], while Rich et al. (2017) measured the iron-based metallicity [Fe/H]. But if we ignore this, our results agree within the uncertainties. Furthermore, we observed the same trend, with increasing metallicity from Id134 ([M/H] = 0.19 dex) over Id1011914 (0.23 dex) to Id3021083 (0.56 dex).

3.5 Completeness

The observations were taken at different nights at different conditions and exposure times. Thus, we expect that the different fields have a different depth. Also, the foreground extinction varies over the different fields, meaning that we can observe deeper into the Galactic Centre and reach intrinsic fainter stars in regions with less extinction. Another factor is crowding, we did not extract spectra of stars that had a close neighbour in order to obtain a clean aperture extraction, and this concerns less stars in the outer part of the cluster. These factors have to be considered when comparing the stellar populations in different regions.

In order to estimate the completeness, we compared the cumulative distribution of observed $K_{\rm S}$ of our sample with the $K_{\rm S}$ distribution of the photometric catalogue. Our sample contains only stars for which we could extract a spectrum with sufficiently high signal-to-noise ratio to measure stellar parameters (see Section 3.3), which leaves only ∼740 stars, including foreground stars. The photometric catalogue can be considered complete compared to our spectroscopic sample, as it is almost 100 per cent complete at $K_{\rm S} = 15$ mag beyond the central parsec (Nogueras-Lara et al. 2018). For the different KMOS mosaic regions, we compared the photometric distributions and determined the $K_{\rm S}$ magnitude at which our sample is 50 per cent complete. The resulting magnitudes are listed in Table 2. We determined the uncertainty of 0.1 mag by trying different bin sizes of the photometric histograms and using the standard deviation as uncertainty. The completeness may not be constant over a given field, as some regions were observed only once due to inactive IFUs and other regions were observed twice. Our completeness limits are therefore averages for a given field. Most fields reach the 50 per cent completeness limit at 11.9–12.3 mag. Only Field 2 has a higher completeness, reaching 12.5 mag. We also consider the mean extinction $\langle A_{K_{\rm S}} \rangle$ of our stars in each field and correct the $K_{\rm S}$ completeness limit. This is not a measure of an extinction-corrected completeness but allows a rough estimate of the completeness variation in the different fields. With the mean extinction correction, the completeness ranges from 9.53 to 10.25 mag for Fields 1–2, while Fields 3–6 are rather comparable, with 9.71–9.94 mag.

We note that Field 0 reaches the 50 per cent completeness limit at 13.7 mag (measured beyond the extremely dense central $r < 0.5$ pc), despite the shorter exposure time. This is caused by the different extraction method, which allows to extract faint stars nearby bright stars. However, this method was not feasible for the Fields 1–6 (see Section 2.2).

Table 2. Completeness of analysed sample.

Field	$K_{\rm S}$ 50% complete (mag)	$K_{\rm S}$ 50% complete - $\langle A_{K_{\rm S}} \rangle$ (mag)	$<K_{\rm S}>$ (mag)	$\langle A_{K_{\rm S}} \rangle$ (mag)
1	11.9 ± 0.1	9.53	11.7	2.38
2	12.5 ± 0.1	10.25	12.2	2.27
3	11.9 ± 0.1	9.67	11.8	2.23
4	12.3 ± 0.1	9.87	12.0	2.44
5	12.2 ± 0.1	9.94	12.0	2.27
6	12.2 ± 0.1	9.71	11.7	2.44
0	13.7 ± 0.1	11.42	13.1	2.28

4 RESULTS

We measured the overall metallicity [M/H] of a sample of 649 stars in the Milky Way's nuclear star cluster at projected radii of 0.4–4.9 pc from the central supermassive black hole. The stars are located towards the Galactic north-west and south-east and spread out over an area of >22 pc^2. We will publish a table of our stellar parameter measurements online.

4.1 Stellar parameter distributions

We show the stellar parameter distribution for 649 stars, which are likely cluster members based on their photometry or spectral slope, in Fig. 4. The mean, median, and standard deviation values of the $T_{\rm eff}$, [M/H], and log (g) distributions are denoted on the plots. The error bars denote the mean statistical and total uncertainties for the stellar parameter measurements. A comparison with Field 0 stars (fig. 4 of Feldmeier-Krause et al. 2017a) reveals that the mean values of the distributions are similar. The $T_{\rm eff}$ distribution is

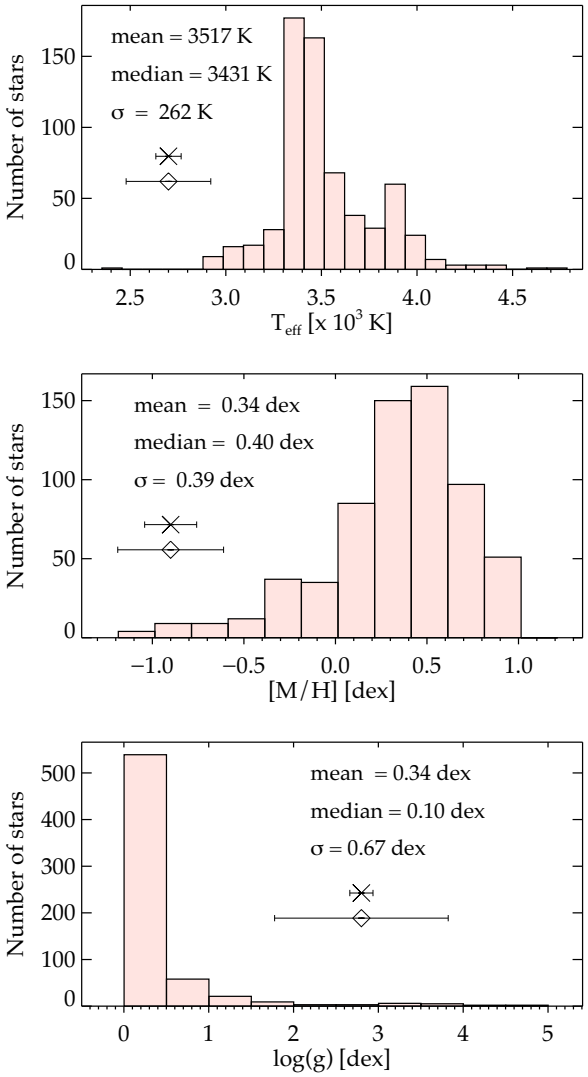

Figure 4. Histograms of the stellar parameters for 649 stars with intrinsic colour within $(H - K_S)_0 = (-0.5$ mag; 0.8 mag) and observed colour $H - K_S > 1.3$ mag. From top to bottom: effective temperature $T_{\rm eff}$, metallicity [M/H] and surface gravity $\log(g)$. Mean, median, and standard deviation of the distributions are noted as legend in the respective panels. The error bars denote the mean statistical uncertainty (cross symbol) and the mean total uncertainty (diamond symbol) of the measurements.

slightly narrower (by 34 K) and cooler (by a mean $T_{\rm eff}$ of 130 K). The reason is probably that Field 0 contains a larger fraction of fainter, slightly hotter stars. The metallicity distribution has a higher mean value of [M/H] = 0.34 dex than Field 0 (0.26 dex) and is slightly narrower ($\sigma_{\rm [M/H]} = 0.39$ dex instead of 0.42 dex in Field 0). The surface gravity has the largest uncertainties and has also slightly lower values and a narrower distribution than Field 0.

4.2 Spatial anisotropy for stars with [M/H] < 0 dex

We show the spatial distribution of the stars in our data set in Fig. 5 on the upper panel and the colours denote different [M/H]. Subsolar metallicity stars with [M/H] < 0.0 dex are highlighted as square symbols. There are more subsolar metallicity stars in the N and NW than in the S and SE.

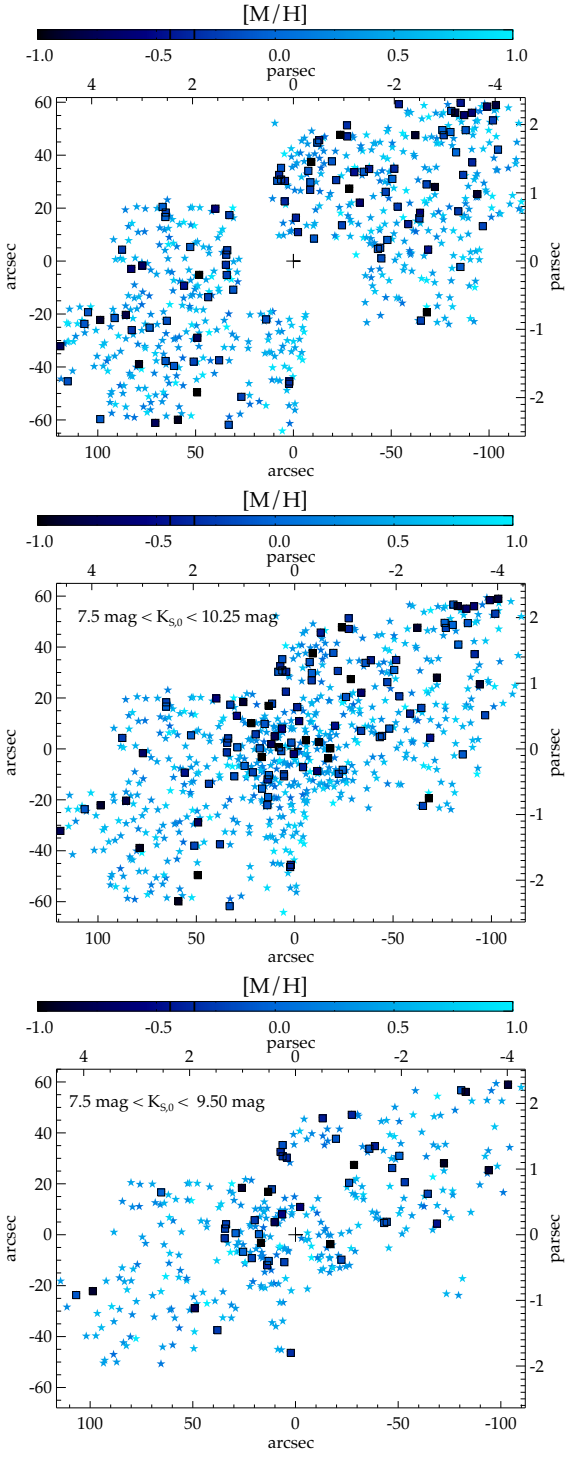

Figure 5. Spatially resolved distribution of the metallicity in offset coordinates from Sgr A∗ (marked as a black plus sign), Galactic north is up. The different colours denote the metallicity [M/H]. Upper panel: 649 stars of our new data set with $(H - K_S)_0 = (-0.5$ mag; 0.8 mag) and $H - K_S > 1.3$ mag; middle panel: including the data of Feldmeier-Krause et al. (2017a), but using only the 729 stars with extinction-corrected K-band magnitudes $K_{S,0}$ in the range of 7.5–10.25 mag; lower panel: 344 stars with extinction-corrected K-band magnitudes in the range of 7.5–9.5 mag and after applying cuts as described in the text. We highlight subsolar metallicity stars with [M/H] < 0.0 dex with square symbols, they are predominantly located in the centre and towards the north.

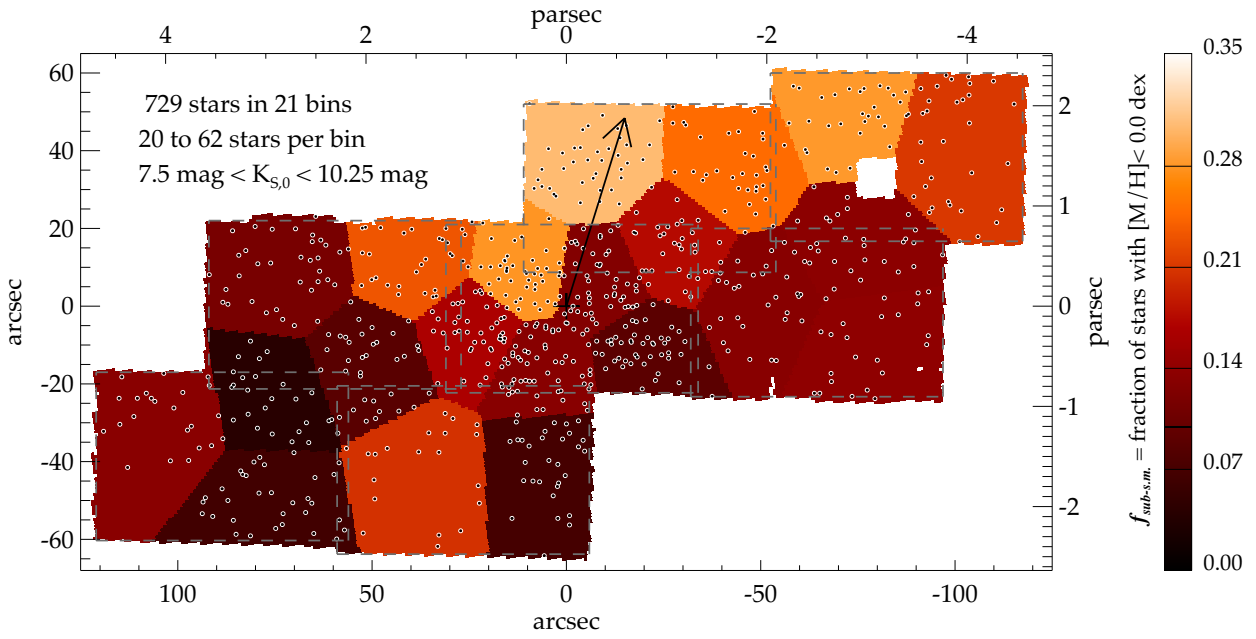

Figure 6. Binned map of the fraction of stars with [M/H] < 0.0 dex $f_{\text{sub-s.m.}}$ per bin in Galactic coordinates offset from Sgr A∗. Bright orange colours denote a larger fraction of subsolar metallicity stars. We also plot the stars in each bin as black points with white circles. The extent of the different fields is illustrated by grey dashed lines. The black arrow denotes the gradient of the fraction. The map was resampled such that one resolution element corresponds to four KMOS spatial pixels, i.e. 0.8 arcsec. The white field in the upper right is a hole caused by a technical problem during observations. We find a gradient of the fraction of subsolar metallicity stars, with a larger fraction located in the Galactic north.

To confirm this finding and quantify the anisotropic distribution of subsolar metallicity stars, we corrected for the varying completeness (Table 2) of the data by applying a brightness cut to our sample. We considered stars with only an extinction-corrected $K_{S,0}$ < 10.25 mag. Applying this cut allows us to include the data from Feldmeier-Krause et al. (2017a), which have a higher completeness than our data. We excluded rather young supergiant stars by considering only stars with $K_{S,0}$ > 7.5 mag. Our final sample contains 729 stars, which are mostly red giant stars, and potentially asymptotic giant branch stars. The spatial distribution of these stars is shown in the middle panel of Fig. 5.

To investigate spatial variations of the metallicity distribution, we binned our sample with a modified version of the Voronoi binning code of Cappellari & Copin (2003). The original procedure performs spatial binning of two-dimensional data such that each bin is relatively round and has approximately the same signal-to-noise ratio, given a minimum S/N. Our code distributes the stars such that we have approximately the same number of stars in a bin. We tried different realizations, with a different minimum number of stars (20, 25, and 30), and obtained consistent results.

For each spatial bin, we calculated the fraction of stars with [M/H] < 0.0 dex, $f_{\text{sub-s.m.}}$. This fraction is more sensitive to the tail of subsolar metallicity stars in the metallicity distribution than the mean or median metallicity. We show a map of the subsolar metallicity star fraction $f_{\text{sub-s.m.}}$ in Fig. 6. There is an increase of $f_{\text{sub-s.m.}}$ to the Galactic north and west, indicated by lighter colours. We also computed the gradient of the subsolar metallicity star fraction, indicated as black arrow in Fig. 6. In Galactic coordinates, the position angle of the metallicity fraction gradient is at about 340° (in equatorial coordinates 309°) east of north and the slope is 2 per cent per 10 arcsec.

We tested the robustness of our metallicity fraction gradient by applying several additional selection criteria to our sample of stars. In particular, we excluded the stars for which we do not have coverage by the extinction map, located in the Galactic south at y < −50 arcsec in our maps. These stars were classified as member stars using machine learning in Section 3.3. Further, the extinction map may have systematic uncertainties in regions with high extinction and underestimate the extinction in those regions. This can cause that foreground stars are considered as member stars. To detect such regions, we used J-band photometry, which is more affected by extinction than the K-band. We created a J-band number density map n_J using the J-band catalogue of stars by Nogueras-Lara et al. (2018). Regions with low number density n_J of J-band sources indicate higher extinction. We excluded about 120 stars that are in regions where n_J is less than the mode of the n_J map. Both steps exclude stars in regions with rather high extinction. Our data set also contains stars with a rather low extinction. In our two-layer extinction correction, we used a different extinction map for about 40 stars with observed 1.3 mag < $(H - K_S)$ < 1.7 mag. We also tested excluding these stars from our sample. All these cuts together reduce our sample from 729 to 562 stars and the number of stars with [M/H] < 0 dex from 115 to 88. Further, we tested a more stringent cut of $K_{S,0}$ < 9.5 mag instead of 10.25 mag, which decreased the number of stars by 40 per cent. All these additional cuts and criteria do not affect our main results. In all cases, the metallicity fraction gradient points to about 330°–350° east of north. The gradient of the median extinction, however, varies, depending on our sample of stars. This can be expected, as we excluded stars located in regions of high and low extinction.

Further, we tested whether it is possible that the stars, randomly distributed over the observed field, produce the observed steepness of the metallicity fraction gradient. Using our sample of 729 stars, in 5000 runs we shuffled the values of [M/H], calculated the $f_{\text{sub-s.m.}}$ in the same 21 bins as in Fig. 6, and measured the metallicity fraction gradient. The median metallicity fraction gradient of the 5000 runs

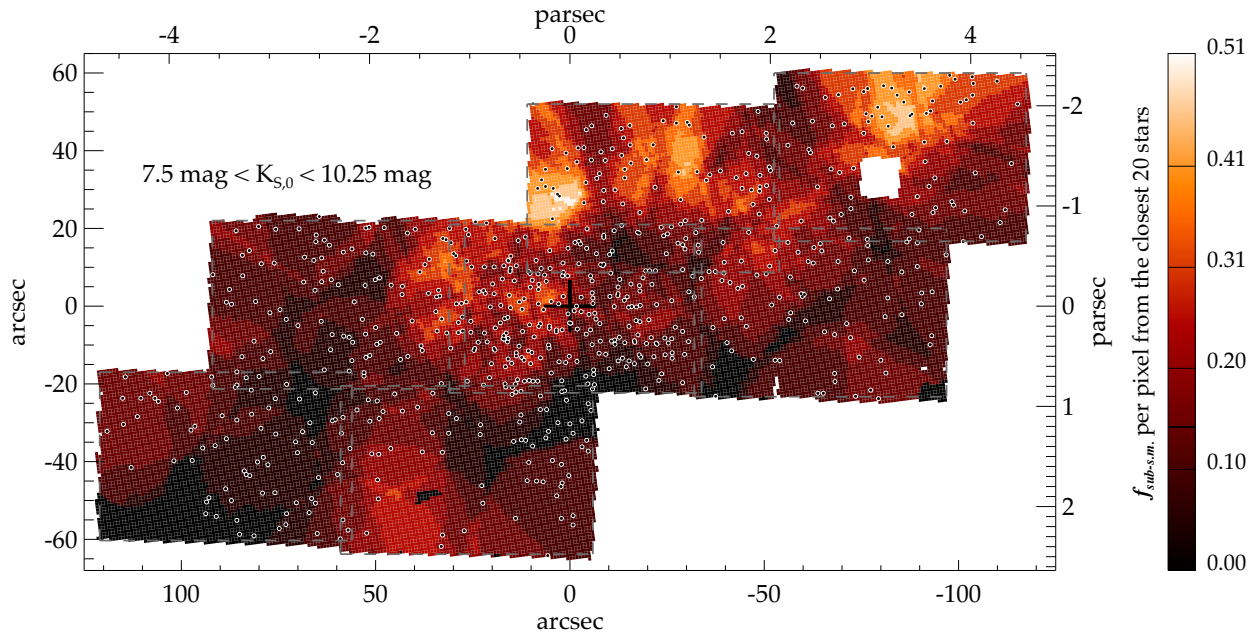

Figure 7. Map of the fraction of stars with [M/H] < 0.0 dex, among the 20 closest stars in each pixel. Coordinates, symbols, and sampling as in Fig. 6. However, the colour bar has a different range. The fraction of subsolar metallicity stars is increasing towards the north of our field.

is 0.52 per cent per 10 arcsec. Only 0.04 per cent, i.e. two out of 5000 runs, result in a metallicity fraction gradient of ≥2 per cent per 10 arcsec, comparable to our data. Thus, it is unlikely that our observation is caused by statistical fluctuations.

For a finer spatial resolution, we searched for the 20 closest stars of each 0.2 arcsec × 0.2 arcsec pixel in our field. From these 20 stars, we computed the fraction of stars with [M/H] < 0.0 dex, $f_{\text{sub-s.m.}}$. The result is shown in Fig. 7, adjacent pixels are correlated, and the spatial resolution depends on the stellar number density in a given region. Nevertheless, the resolution is finer than in Fig. 6. The general appearance of the maps is similar, with higher fractions of subsolar metallicity stars in the north. This confirms that the metallicity distribution variation is not caused by spatial binning.

4.3 Metallicity and radial velocity distributions in different regions of the nuclear star cluster

We found an asymmetry in the distribution of subsolar metallicity stars, with a larger fraction of [M/H] < 0 dex in the Galactic north and west of the nuclear star cluster compared to the south and east. In this section, we investigate whether the change of the subsolar metallicity star fraction is due to a global shift of the metallicity distribution, or caused by a low-metallicity tail in the metallicity distribution.

We selected stars in the Voronoi bins (Fig. 6) with $f_{\text{sub-s.m.}}$ >20 per cent as low-metallicity group and stars in the bins with $f_{\text{sub-s.m.}}$ < 10 per cent as high-metallicity group. The two groups contain 211 and 169 stars. We show the two different normalized metallicity distributions in Fig. 8. The metallicity distribution in the region with a higher fraction of subsolar metallicity stars has a low-metallicity tail at [M/H] < 0.0 dex. We fitted a Gaussian function to the metallicity distributions. In the high-metallicity region, the Gaussian is located at [M/H] = 0.39 dex with σ = 0.3 dex. This distribution is reasonably well represented by a Gaussian function. For the metallicity distribution in the low-metallicity region, we

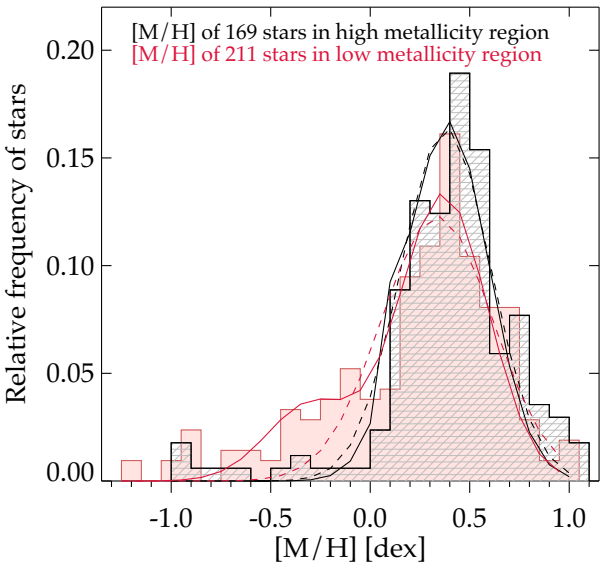

Figure 8. Normalized metallicity distribution of stars in the high-metallicity region (black colour, fraction of subsolar metallicity stars $f_{\text{sub-s.m.}}$ < 10 per cent) and low-metallicity region (red, fraction of subsolar metallicity stars $f_{\text{sub-s.m.}}$ > 20 per cent). The black dashed line denotes a Gaussian fit to the metallicity distribution of the high-metallicity region; the red dashed line of the low-metallicity region; and the red solid line a double-Gaussian fit of the low-metallicity region. The double-Gaussian fit is required to fit the tail of subsolar metallicity stars.

obtained a Gaussian located at [M/H] = 0.34 dex with σ = 0.4 dex. However, the tail of subsolar metallicity stars with [M/H] < 0.0 dex led us to perform a double Gaussian fit to the metallicity distribution in the low-metallicity region. The higher peak is located at 0.37 dex with σ = 0.3 dex; the second, low-metallicity peak at [M/H] = −0.29 dex and σ = 0.3 dex. The exact results of the Gaussian fits

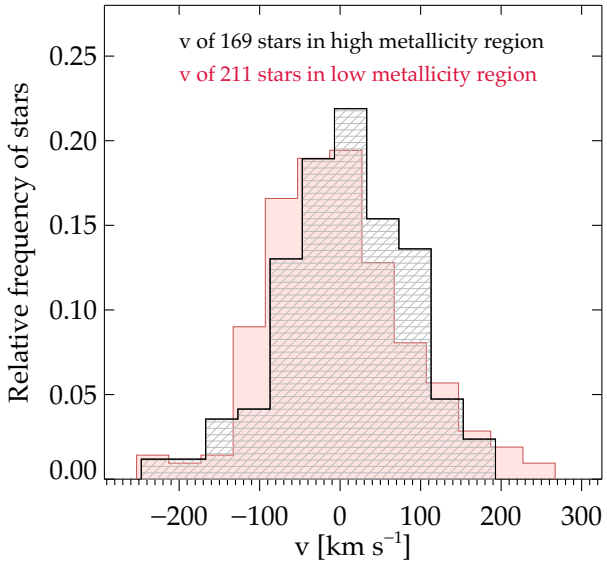

Figure 9. Normalized radial velocity distribution of stars in the high-metallicity region (black colour, fraction of subsolar metallicity stars $f_{\text{sub-s.m.}} < 10$ per cent) and low-metallicity region (red, fraction of subsolar metallicity stars $f_{\text{sub-s.m.}} > 20$ per cent).

depend on the binning of the histograms. But irrespective of the binning, the metallicity distribution in the low-metallicity region is better described by a double-Gaussian distribution than a single Gaussian.

The histograms indicate that there are metal-rich populations of stars in both regions, with similar Gaussian distributions, located at [M/H] $\approx$ 0.38 dex with $\sigma \approx$0.3 dex. In both regions, there are also subsolar metallicity stars. However, the Galactic north-western region of the nuclear star cluster contains a larger relative frequency subsolar metallicity stars. The nuclear star cluster's stellar populations are not homogeneous and not isotropic around Sgr A∗.

We also plot histograms of the radial velocity of stars in the high-metallicity and low-metallicity regions in Fig. 9. The mean velocities differ by 10 km s^{-1}, which may be due to the different locations of the regions and the rotation of the nuclear star cluster. The velocity dispersion in the low-metallicity region is higher by 9 km s^{-1}. Although the mean projected distances of the stars in the two regions are similar (∼55 arcsec), we cannot exclude that the velocity dispersion difference is caused by the spatial distribution of the stars. A more detailed kinematic analysis is required, but this is beyond the scope of this paper. We publish the radial velocity measurements with our stellar parameters online.

4.4 A low fraction of metal-poor stars with [M/H] < −0.5 dex

So far we consider subsolar metallicity stars with [M/H] < 0 dex. We chose this cut because we found that the metallicity distribution in different spatial regions varies at [M/H] < 0.0 dex (see Section 4.3). Other publications considered metal-poor stars in the Galactic center as stars with [M/H] < −0.5 dex and computed the metal-poor star fraction. In order to enable a comparison with the literature, we use the criterion [M/H] < −0.5 dex for metal-poor stars in this section. We note that this definition deviates from the classification suggested by Beers & Christlieb (2005), where metal-poor stars have −2.0 dex < [Fe/H] ≤ −1.0 dex.

In the entire area covered by Fields 1–6, we obtain $f_{\text{mp}} = 3.5$ per cent. Do et al. (2015) found that 6 per cent of their stars located at projected radii $r < 0.5$ pc have [M/H] < −0.5 dex; Feldmeier-Krause et al. (2017a) obtained a similar value in the central Field 0 with $r < 1.4$ pc, 5.2 per cent. We tested if the lower fraction in our data compared to Field 0 in Feldmeier-Krause et al. (2017a) is due to our lower completeness rather than the different spatial coverage. We made magnitude cuts and considered stars with only 7.5 mag < $K_{\text{S},0}$ < 10.25 mag. After this cut, the fractions of stars with [M/H] < −0.5 dex change only little, and the discrepancy between Field 0 and the combined Fields 1–6 remains. We also tested if there are spatial variations of f_{mp} with [M/H] < −0.5 dex in Fields 1–6, but since the total number of stars with [M/H] < −0.5 dex is only 20, we are more sensitive to binning and data selection effects; therefore, the following results need to be considered with care. We found that f_{mp} has a much shallower gradient than for [M/H] < 0 dex, changing only by about 0.2 per cent per 10 arcsec instead of 2 per cent per 10 arcsec. The direction of the gradient is in agreement with the gradient for [M/H] < 0.0 dex, with a larger f_{mp} towards the north, at about 340° east of north.

5 DISCUSSION

5.1 Metallicity distributions in the literature

In agreement with our previous work (Feldmeier-Krause et al. 2017a), where we studied stars in the nuclear star cluster out to 1.4 pc, we found that the majority of stars are metal-rich. Also, Do et al. (2015) found a large fraction of metal-rich stars in the central 1 pc of the Galactic Centre and in addition stars with [M/H] $\lesssim$ 0 dex.

Ryde & Schultheis (2015) measured [Fe/H] for 9 M giants in the Galactic Centre but at larger projected distances from Sgr A∗ than our data. Their data set was metal-rich, with a mean [Fe/H] = 0.11 ± 0.15 dex. The data were re-analysed by Nandakumar et al. (2018), who found an even higher mean [Fe/H] of 0.3 dex. Rich et al. (2017) obtained the so far largest sample at high spectral resolution ($R \sim 24\,000$), with 17 M giants in the nuclear star cluster and nuclear disc. They obtained a mean iron-based metallicity of [Fe/H] = −0.11 dex (median [Fe/H] = −0.16 dex) for their 17 stars, ranging from −1.15 to +0.64 dex. This is a lower mean value than we obtain; however, there are several differences in our sample and analysis. Rich et al. (2017) used the iron-based metallicity [Fe/H], while we used the overall metallicity [M/H], meaning that all elements are considered, not only Fe. Further, we have different assumptions on [α/Fe]. Rich et al. (2017) assumed [α/Fe] = 0.3 dex for stars with [Fe/H] = −0.5 dex, with [α/Fe] decreasing linearly with increasing [Fe/H] up to [Fe/H] = 0 dex, and [α/Fe] = 0 dex at [Fe/H] > 0 dex, whereas we assumed that [α/Fe] = 0 dex at all values of [M/H]. This causes differences for stars with subsolar metallicity. Concerning the sample of stars, the median K_{S} magnitude of Rich et al. (2017) is 1 mag brighter than our median K_{S}.

For few giant stars in the nuclear star cluster, a detailed abundance analysis was performed so far. Ryde et al. (2016) studied a high-resolution spectrum ($R \sim 24\,000$) of a metal-poor giant star in the Galactic Centre and found [Fe/H] ≈ −1.0 dex and [α/Fe] ≈ 0.4 dex, which confirms the presence of metal-poor giant stars in the Galactic Centre region with high spectral resolution data. Do et al. (2018) investigated the other extreme of the metallicity distribution and observed metal-rich stars of the nuclear star cluster with high spectral resolution ($R \sim 25\,000$). They confirmed the high value of the overall metallicity [M/H] found with medium-resolution data (Do et al. 2015) for one of the stars. But they also found that model

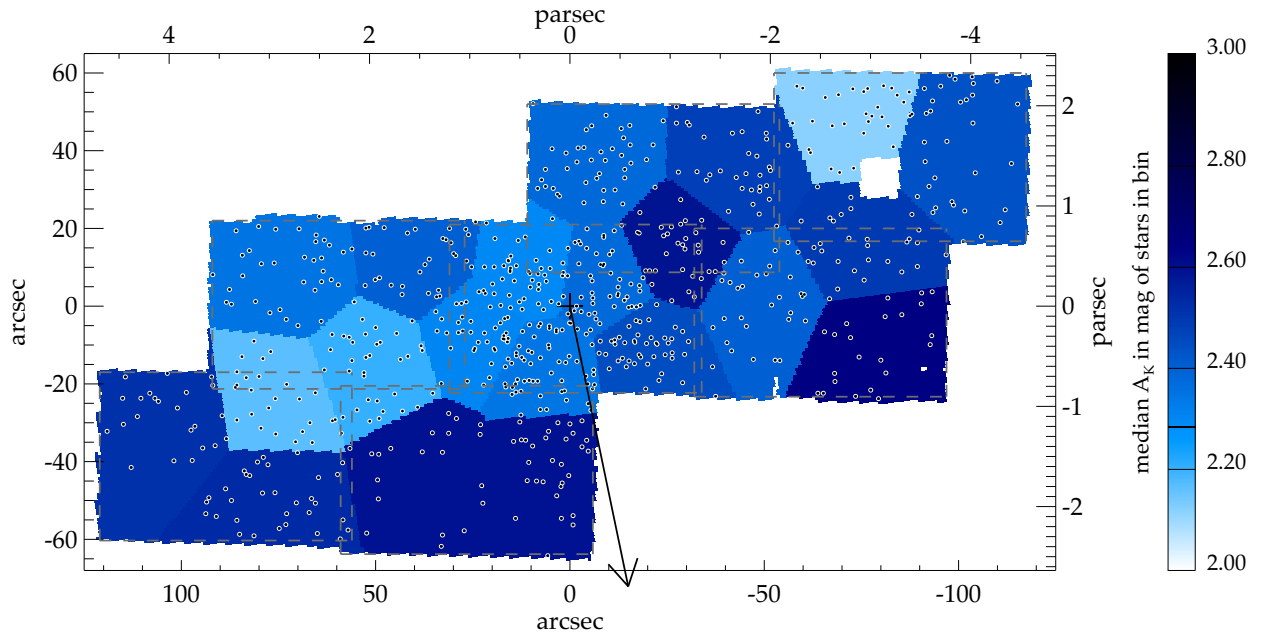

Figure 10. Binned map of the median extinction A_K of the stars in each bin. Darker colours denote a higher median extinction. The black arrow denotes the gradient of the median extinction. Coordinates, symbols, and sampling as in Fig. 6. The median extinction per bin is not correlated with the fraction of subsolar metallicity stars.

spectra cannot reproduce all features of metal-rich stars. This may affect also the accuracy of our results at supersolar metallicities. As noted in Section 3.4, the systematic uncertainties for metal-rich stars [M/H] > 0.3 dex may be underestimated.

Our fraction of metal-rich stars with [M/H]$\geq$0.3 dex $f_{\rm mr}$ is 0.6. Nandakumar et al. (2018) obtained $f_{\rm mr} = 0.4$, and Rich et al. (2017) obtained $f_{\rm mr} = 0.2$. Do et al. (2015), who have a more concentrated sample located within 1 pc of the nuclear star cluster, found a higher fraction of $f_{\rm mr} = 0.7$.

In summary, our larger data set confirms what has been found in previous studies with smaller samples: The nuclear star cluster has not only a high fraction of metal-rich stars [M/H] > 0 dex but also a non-negligible number of subsolar metallicity stars. Differences to other studies are caused by different assumptions, methods, and samples.

5.2 Extinction and completeness effects

Extinction in the Galactic Centre is high and variable, with A_K ranging from $\lesssim$1.6 to $\gtrsim$3.2 mag. Local changes in the extinction can mean that our stellar spectra lie deeper within the nuclear star cluster or mostly in the outer regions. We cannot say for sure where a given star is, as we do not know individual distances. However, by looking at the median extinction in our Voronoi bins, we can at least test if a region has higher extinction, and a dark cloud along the line-of-sight may prevent a deeper look into the nuclear star cluster. We calculated the median extinction of the stars in a Voronoi bin with the extinction maps of Nogueras-Lara et al. (2018). The results are shown in Fig. 10, with the same binning as in Fig. 6. The median extinction values range from 2.1 to 2.6 mag but are not correlated with the fraction of subsolar metallicity stars shown in Fig. 6. We also computed a gradient, shown as black arrow in Fig. 10, and found that it is approximately 150° offset to the metallicity fraction gradient. The gradient changes with binning, within a range of 45°.

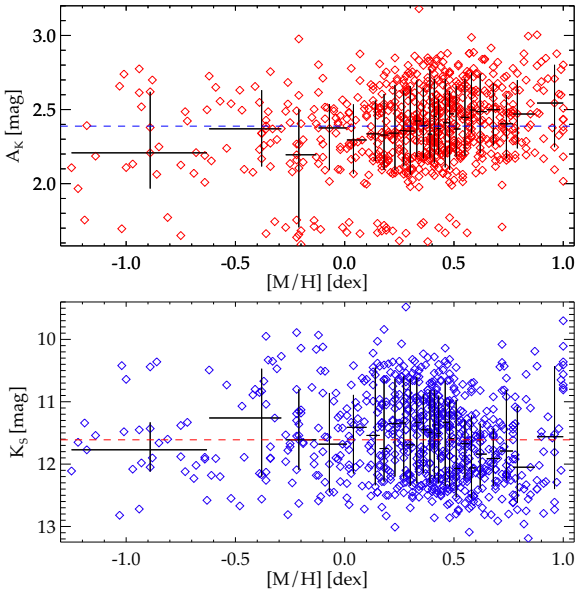

Figure 11. Stellar metallicity of 729 stars plotted against their local extinction A_K (upper panel) and observed K_S magnitude (lower panel). The horizontal dashed lines denote the overall median values of A_K and K_S, while the black data points denote the median values of A_K and K_S for 30 stars, sorted by [M/H]. The horizontal black lines show which range of [M/H] a given bin spans and the vertical black lines denote the 33. and 67. percentiles.

The reason is that extinction varies on smaller scales than the size of our Voronoi bins.

We also analysed the stellar metallicity [M/H] as a function of the extinction A_K for each star individually (Fig. 11, upper panel). The values for A_K have a gap, with few stars having A_K between 1.8 and 2.0 mag. This is due to our two-layer extinction

correction (Section 3.3), where we applied different extinction maps for stars with different observed colour $H - K_S$. We also plot the median extinction for 30 stars, sorted by their value of [M/H], as black crosses. The vertical error bar denotes the 33. and 67. percentile of the A_K distributions. All bins lie well within the median extinction of all stars (horizontal dashed line). There may be a mild correlation between [M/H] and A_K, such that stars with lower [M/H] are in regions with lower A_K, but the variation of the median A_K is only 0.35 mag. A linear fit to the median A_K as a function of [M/H] has a slope of 0.16 ± 0.13 mag dex^{-1}. When we apply additional cuts to remove stars in regions with high and low extinction regions, as in Section 4.2, the relation disappears and the slope is 0.07 ± 0.1 mag dex^{-1}. This shows that there is no significant correlation of [M/H] and A_K, and our results of the spatial anisotropy of subsolar metallicity stars are not caused by variable extinction.

Likewise, the varying completeness over the field of view of our data is unlikely to cause the change in the fraction of subsolar metallicity stars $f_{\text{sub-s.m.}}$. We made magnitude cuts to ensure that the faint population of stars, which is distributed unevenly among fields due to varying completeness, do not bias our results. All fields contain stars in the same magnitude range. Also, the Fields 1 and 2 in the north and north-west, which have a high fraction of subsolar metallicity stars, have very different completeness (see Table 2) and they are the fields with the lowest and highest completeness (with exception of the central field). Yet, both fields contain a higher fraction of subsolar metallicity stars than other fields, with completeness values in between. We conclude that varying completeness does not cause the variation of the subsolar metallicity star fraction.

5.3 Data selection effects

We tested whether we introduce any bias in the distribution of subsolar metallicity stars when we deselect stars with low S/N and bad fit quality. First, we tested if the subsolar metallicity stars are significantly fainter than metal-rich stars, which would suggest that they are more likely to be deselected. We show the stellar metallicity [M/H] as a function of the observed *K*-band magnitude K_S (Fig. 11, lower panel). We found no correlation of [M/H] with K_S; a linear fit to the median K_S as a function of [M/H] gives a slope of 0.06 ± 0.29 mag dex^{-1}. This means that the subsolar metallicity stars are not significantly brighter or fainter than metal-rich stars in our sample, an effect that might be caused by a biased sample selection.

Further, we investigated the spectra that were deselected for our analysis. For each field, we stacked spectra of stars with $5 < \text{S/N} < 20$ and applied full spectral fitting to the six stacked spectra. If the stacked spectra in the Fields 4–6 had a lower metallicity than the spectra in the Fields 1–2, this would suggest that we deselected subsolar metallicity stars in the south or metal-rich stars in the north and introduced a bias. Before stacking the spectra, we used their radial velocities measured in Section 3 with PPXF to shift them to rest wavelength. We summarize our results in Table 3. The number of stars per stack varies from 27 to 96, but most fields have 47 to 68 stars that we used for stacking. The median of the extinction-corrected $K_{S,0}$ magnitude of the stacked stars is fainter than our sample of stars, which we constrained to $K_{S,0} < 10.25$ mag. The stacked spectra in all six fields have supersolar metallicity, which confirms that the nuclear star cluster is metal-rich, also for fainter stars. While there is some variation of the resulting metallicity for the six fields, we find no trend to lower metallicities in Fields 4–6 compared to Fields 1–2, which suggests that we do not introduce a bias to the fraction of subsolar metallicity stars when we perform out data selection.

Table 3. Summary of stacked spectra.

Field	Number of stacked spectra	Median $K_{S,0}$ (mag)	(M/H) (dex)	σ_{fit} (dex)	σ_{fit} (dex)
1	62	11.9	0.07	+0.03	−0.02
2	96	12.5	0.13	+0.03	−0.02
3	47	11.7	0.18	+0.02	−0.02
4	68	11.3	0.24	+0.02	−0.02
5	60	12.4	0.13	+0.02	−0.02
6	27	10.6	0.31	+0.01	−0.02

5.4 Possible origin of the metallicity asymmetry

The formation of nuclear star clusters is still under debate. It has been proposed that (a) the stars formed '*in situ*', i.e. in the Galactic Centre (e.g. Milosavljević 2004; Pflamm-Altenburg & Kroupa 2009); or (b) a 'wet merger' scenario, where massive star clusters formed in the Galactic disc, and migrated to the centre while continuing to form stars from their gas reservoir (Guillard, Emsellem & Renaud 2016); or (c) a 'dry merger' scenario, where star clusters formed 'ex situ', migrated to the Galactic Centre through dynamical friction, and merged to the nuclear star cluster (e.g. Tremaine, Ostriker & Spitzer 1975; Antonini et al. 2012; Arca-Sedda et al. 2015; Arca-Sedda & Gualandris 2018). These scenarios are able to produce the observed mixed stellar populations (Perets & Mastrobuono-Battisti 2014; Aharon & Perets 2015; Guillard et al. 2016) and thus also a broad metallicity distribution.

The spatial anisotropy of subsolar metallicity stars may indicate that some of them were brought to the Galactic Centre from star cluster infall events. Perets & Mastrobuono-Battisti (2014) studied the distribution of stellar populations in *N*-body simulations of repeated star cluster infall events. The infalling star clusters resemble massive globular clusters in their density distribution and start at an orbital radius of 20 pc (Antonini et al. 2012). The simulation shows that the different stellar populations originating from the star clusters have distinct three-dimensional structures, and some structures are highly anisotropic even Gyr after their infall. Similar simulations were performed in Arca-Sedda, Kocsis & Brandt (2018), and they found that the initial spatial distribution is determined by the orbit of the infalling star cluster.

The infall time of the star clusters depends on the mass and distance to the nuclear star cluster. For example, a cluster with mass 10^5–10^7 $M_\odot$ and starting at $r \sim 2$–5 kpc could have reached the Galactic Centre < 3 Gyr ago, just as an infalling dwarf galaxy with initially a few 10^8–10^{10} $M_\odot$ and starting at *r* between a few 10 to a few hundred kpc (Arca-Sedda et al. in preparation). The Milky Way has several globular star clusters located in the Galactic bulge. Within a galactic-centric radius of 2 kpc, almost 50 per cent of the clusters have [Fe/H] > −1.0 dex and about 20 per cent even [Fe/H] > −0.5 dex (Harris 1996, 2010). However, the census of Galactic globular clusters is not yet complete, and new clusters were discovered recently (Camargo 2018; Camargo & Minniti 2019).

More information is required to determine the origin of subsolar metallicity stars in the nuclear star cluster. If some of them originate from a star cluster infall, they should have the same metallicity and element abundances. Our metallicity measurements have large uncertainties of $\sigma_{[\text{M/H}]} \approx 0.26$ dex, which is larger than the internal

metallicity dispersion of Galactic globular clusters. We require high-resolution spectroscopy and precise element abundance measurements to confirm the hypothesis that a star cluster infall caused the spatial anisotropy of subsolar metallicity stars. If several infall events happened, element abundance measurements may be able to separate the different stellar populations further, and their common chemistry will show which stars likely formed together.

Another way to investigate the origin of the metallicity asymmetry is to combine the metallicities with kinematic measurements, i.e. radial velocities and proper motions. If indeed a star cluster or dwarf galaxy infall to the nuclear star cluster happened not longer ago than the relaxation time, the population can be distinguished from its kinematic properties, as shown in Arca-Sedda et al. (in preparation) using *N*-body simulations. Distinct kinematics were indeed found by Do et al. (in preparation) for subsolar metallicity stars located in the central Field 0. Future analysis can reveal if also the subsolar metallicity stars found in this study show distinct kinematics from the supersolar metallicity stars. To enable such an analysis, we publish the radial velocity measurements with our stellar parameters online.

6 CONCLUSIONS

We observed almost half of the area of the Milky Way's nuclear star cluster with the integral-field spectrograph KMOS. We extracted *K*-band spectra of more than 600 late-type stars and derived stellar parameters using full-spectral fitting. Most stars are red giant stars, with metallicities ranging from [M/H] $= -1.25$ dex to $> +0.3$ dex. We investigated the spatial distribution of subsolar metallicity stars with [M/H] < 0.0 dex. The Galactic north and north-west region of our observed field has more than two times larger fraction of subsolar metallicity stars than the region in the Galactic south-east. A comparison of the metallicity histograms in the two regions revealed a tail of stars with [M/H] < 0.0 dex in the low-metallicity region. One possible explanation for such an anisotropic metallicity distribution is a recent merger event of a subsolar metallicity stellar population, which has not yet mixed completely with the more metal-rich stars of the nuclear star cluster.

ACKNOWLEDGEMENTS

We would like to thank the ESO staff who helped us to prepare our observations and obtain the data. We are grateful to Lodovico Coccato and Yves Jung for advice and assistance in the data reduction process. We thank Barbara Lanzoni for sharing her SINFONI data of NGC 6388. We also thank the referee for useful comments and suggestions.

N. N. and F. N.-L. gratefully acknowledge funding by the Deutsche Forschungsgemeinschaft (DFG, German Research Foundation) – Project-ID 138713538 – SFB 881 ('The Milky Way System', subproject B8). The research leading to these results has received funding from the European Research Council under the European Union's Seventh Framework Programme (FP7/2007-2013) / ERC grant agreement n. [614922] (RS and FNL). R. S. and F. N. L. acknowledge financial support from the State Agency for Research of the Spanish MCIU through the 'Center of Excellence Severo Ochoa' award for the Instituto de Astrofísica de Andalucía (SEV-2017-0709). R. S. acknowledges financial support from national project PGC2018-095049-B-C21 (MCIU/AEI/FEDER, UE). A. C. S. acknowledges financial support from NSF grant AST-1350389. This research made use of the SIMBAD data base (operated at CDS, Strasbourg, France). This research made use of Montage. It is funded by the National Science Foundation under grant number ACI-1440620 and was previously funded by the National Aeronautics and Space Administration's Earth Science Technology Office, Computation Technologies Project, under Cooperative Agreement Number NCC5-626 between NASA and the California Institute of Technology.

Based on observations collected at the European Organisation for Astronomical Research in the Southern Hemisphere, Chile (60.A-9450(A), 091.B-0418, 093.B-0368, 195.B-0283.

REFERENCES

Aharon D., Perets H. B., 2015, ApJ, 799, 185
Antonini F., Capuzzo-Dolcetta R., Mastrobuono-Battisti A., Merritt D., 2012, ApJ, 750, 111
Arca-Sedda M., Gualandris A., 2018, MNRAS, 477, 4423
Arca-Sedda M., Capuzzo-Dolcetta R., Antonini F., Seth A., 2015, ApJ, 806, 220
Arca-Sedda M., Kocsis B., Brandt T. D., 2018, MNRAS, 479, 900
Beers T. C., Christlieb N., 2005, ARA&A, 43, 531
Blum R. D., Sellgren K., Depoy D. L., 1996, AJ, 112, 1988
Blum R. D., Ramírez S. V., Sellgren K., Olsen K., 2003, ApJ, 597, 323
Bressan A., Marigo P., Girardi L., Salasnich B., Dal Cero C., Rubele S., Nanni A., 2012, MNRAS, 427, 127
Buchner J. et al., 2014, A&A, 564, A125
Camargo D., 2018, ApJ, 860, L27
Camargo D., Minniti D., 2019, MNRAS, 484, L90
Cappellari M., Copin Y., 2003, MNRAS, 342, 345
Cappellari M., Emsellem E., 2004, PASP, 116, 138
Carr J. S., Sellgren K., Balachandran S. C., 2000, ApJ, 530, 307
Chen Y., Girardi L., Bressan A., Marigo P., Barbieri M., Kong X., 2014, MNRAS, 444, 2525
Cunha K., Sellgren K., Smith V. V., Ramirez S. V., Blum R. D., Terndrup D. M., 2007, ApJ, 669, 1011
Czekaj M. A., Robin A. C., Figueras F., Luri X., Haywood M., 2014, A&A, 564, A102
Davies R. I., 2007, MNRAS, 375, 1099
Davies B., Origlia L., Kudritzki R.-P., Figer D. F., Rich R. M., Najarro F., 2009, ApJ, 694, 46
Davies R. I. et al., 2013, A&A, 558, A56
Do T., Lu J. R., Ghez A. M., Morris M. R., Yelda S., Martinez G. D., Wright S. A., Matthews K., 2013, ApJ, 764, 154
Do T., Kerzendorf W., Winsor N., Støstad M., Morris M. R., Lu J. R., Ghez A. M., 2015, ApJ, 809, 143
Do T., Kerzendorf W., Konopacky Q., Marcinik J. M., Ghez A., Lu J. R., Morris M. R., 2018, ApJ, 855, L5
Dutra C. M., Bica E., 2001, A&A, 376, 434
Feldmeier A. et al., 2014, A&A, 570, A2
Feldmeier-Krause A. et al., 2015, A&A, 584, A2
Feldmeier-Krause A., Kerzendorf W., Neumayer N., Schödel R., Nogueras-Lara F., Do T., de Zeeuw P. T., Kuntschner H., 2017a, MNRAS, 464, 194
Feldmeier-Krause A., Zhu L., Neumayer N., van de Ven G., de Zeeuw P. T., Schödel R., 2017b, MNRAS, 466, 4040
Feroz F., Hobson M. P., Bridges M., 2009, MNRAS, 398, 1601
Fritz T. K. et al., 2016, ApJ, 821, 44
Frogel J. A., Stephens A., Ramírez S., DePoy D. L., 2001, AJ, 122, 1896
Gazak J. Z. et al., 2015, ApJ, 805, 182
Guillard N., Emsellem E., Renaud F., 2016, MNRAS, 461, 3620
Harris W. E., 1996, AJ, 112, 1487
Harris W. E., 2010,arXiV, 2010arXiv1012.3224H
Husser T.-O., Wende-von Berg S., Dreizler S., Homeier D., Reiners A., Barman T., Hauschildt P. H., 2013, A&A, 553, A6
Kamann S., Wisotzki L., Roth M. M., 2013, A&A, 549, A71
Kerzendorf W., Do T., 2015, starkit: First real release,.
Kunneriath D. et al., 2012, A&A, 538, A127
Lanzoni B. et al., 2013, ApJ, 769, 107

Milosavljević M., 2004, ApJ, 605, L13
Nandakumar G., Ryde N., Schultheis M., Thorsbro B., Jönsson H., Barklem P. S., Rich R. M., Fragkoudi F., 2018, MNRAS, 478, 4374
Nishiyama S. et al., 2006, ApJ, 638, 839
Nogueras-Lara F. et al., 2018, A&A, 610, A83
Nogueras-Lara F. et al., 2019a, A&A, 631, A20
Nogueras-Lara F. et al., 2019b, Nature Astron.,
Paumard T., Maillard J.-P., Morris M., 2004, A&A, 426, 81
Perets H. B., Mastrobuono-Battisti A., 2014, ApJ, 784, L44
Pflamm-Altenburg J., Kroupa P., 2009, MNRAS, 397, 488
Pfuhl O. et al., 2011, ApJ, 741, 108
Ramírez S. V., Sellgren K., Carr J. S., Balachandran S. C., Blum R., Terndrup D. M., Steed A., 2000, ApJ, 537, 205
Requena-Torres M. A. et al., 2012, A&A, 542, L21
Rich R. M., Ryde N., Thorsbro B., Fritz T. K., Schultheis M., Origlia L., Jönsson H., 2017, AJ, 154, 239
Rosenfield P., Marigo P., Girardi L., Dalcanton J. J., Bressan A., Williams B. F., Dolphin A., 2016, ApJ, 822, 73
Ryde N., Schultheis M., 2015, A&A, 573, A14
Ryde N., Fritz T. K., Rich R. M., Thorsbro B., Schultheis M., Origlia L., Chatzopoulos S., 2016, ApJ, 831, 40
Saito R. K. et al., 2012, A&A, 537, A107
Schödel R., Feldmeier A., Kunneriath D., Stolovy S., Neumayer N., Amaro-Seoane P., Nishiyama S., 2014a, A&A, 566, A47
Schödel R., Feldmeier A., Neumayer N., Meyer L., Yelda S., 2014b, Class. Quantum Gravity, 31, 244007
Sharples R. et al., 2013, Messenger, 151, 21
Tang J., Bressan A., Rosenfield P., Slemer A., Marigo P., Girardi L., Bianchi L., 2014, MNRAS, 445, 4287
Tremaine S. D., Ostriker J. P., Spitzer Jr. L., 1975, ApJ, 196, 407
van Dokkum P. G., 2001, PASP, 113, 1420
Wallace L., Hinkle K., 1996, ApJS, 107, 312

SUPPORTING INFORMATION

Supplementary data are available at *MNRAS* online.

Table A1. Stellar parameters: Stellar identification number Id, the coordinates in R.A. and Dec, the stellar parameters $T_{\rm eff}$, [*M*/*H*], log (*g*), and v_z, and extinction-corrected $K_{\rm S}$-band magnitude $K_{\rm S,0}$.

Please note: Oxford University Press is not responsible for the content or functionality of any supporting materials supplied by the authors. Any queries (other than missing material) should be directed to the corresponding author for the article.

APPENDIX A: TABLE OF STELLAR PARAMETERS

Table A1. Stellar parameters: Stellar identification number Id, the coordinates in R.A. and Dec, the stellar parameters $T_{\rm eff}$, [*M*/*H*], log (*g*), and v_z, and extinction corrected $K_{\rm S}$-band magnitude $K_{S,0}$. The full table is available online.

Id	R.A. (°)	Dec (°)	$T_{\rm eff}$ (K)	$\sigma_{T_{\rm eff}}$ (K)	[M/H] (dex)	$\sigma_{\rm [M/H]}$ (dex)	log (*g*) (dex)	$\sigma_{\log(g)}$ (dex)	v_z (km s^{-1})	σ_{v_z} (km s^{-1})	$K_{\rm S,0}$ (mag)
1000002	266.41144	− 29.003521	3458	$^{+305}_{-305}$	− 0.36	$^{+0.25}_{-0.25}$	0.5	$^{+1.2}_{-1.2}$	43.1	$^{+7.8}_{-7.8}$	8.29
1000054	266.41284	− 29.005566	3507	$^{+209}_{-209}$	0.10	$^{+0.24}_{-0.24}$	0.0	$^{+1.0}_{-1.0}$	− 29.0	$^{+3.4}_{-3.4}$	8.53
1000112	266.40930	− 29.002455	3576	$^{+207}_{-207}$	− 0.36	$^{+0.25}_{-0.25}$	0.1	$^{+1.0}_{-1.0}$	41.1	$^{+0.9}_{-0.9}$	8.67
1000123	266.40680	− 29.002874	3744	$^{+255}_{-255}$	0.22	$^{+0.30}_{-0.30}$	0.2	$^{+1.0}_{-1.0}$	90.0	$^{+6.3}_{-6.3}$	11.29
1000149	266.40729	− 29.002579	3259	$^{+252}_{-252}$	0.29	$^{+0.41}_{-0.41}$	1.2	$^{+1.0}_{-1.0}$	53.7	$^{+4.6}_{-4.6}$	8.51
1000183	266.41409	− 29.005821	3373	$^{+206}_{-206}$	0.33	$^{+0.28}_{-0.28}$	0.1	$^{+1.0}_{-1.0}$	15.8	$^{+2.3}_{-2.3}$	8.56
1000196	266.41214	− 29.005774	3123	$^{+244}_{-244}$	− 0.39	$^{+0.25}_{-0.25}$	0.6	$^{+1.1}_{-1.1}$	121.0	$^{+1.4}_{-1.4}$	8.30
1000216	266.40958	− 29.003115	3036	$^{+211}_{-211}$	0.18	$^{+0.27}_{-0.27}$	0.8	$^{+1.0}_{-1.0}$	17.4	$^{+2.4}_{-2.4}$	8.13

This paper has been typeset from a TEX/LATEX file prepared by the author.